A comparative study on denoising strategies for imaging diagnostics data from tokamak plasma experiments

Abstract—**Imaging diagnostics, which offers information about the tokamak plasma edge as well as the plasma interior, facilitates the realization of plasma shape and position, impurity distribution, and Magneto-hydrodynamics (MHD) instabilities. Tomographic reconstruction is one of the powerful tools to analyze imaging diagnostic data. The imaging diagnostic is contaminated with noises with a wide variety of origins. Hence, denoising these images relaxes the computational expenses for the tomographic reconstructions and the edge detection algorithms. In this work, we compare the performance of five different Deep Learning (DL) based techniques (REDNet, MWCNN, PRIDNet, CBDNet, and DnCNN) and six traditional denoising methodologies (Median, Gaussian, Bilateral, Wiener, BM3D, NLM). DL-based methods are trained using a synthetic dataset containing a variety of images where stochastic noises of different distributions have been added. Denoising is performed on a simulated noisy image of the circular tokamak plasma, in the visible range, for tangential viewing geometry. The denoising quality is observed as a function of noise magnitude. The Peak Signal-to-Noise Ratio (PSNR) and Structural Similarity Index (SSIM) values are estimated for each denoising attempt. The comparison suggests that the machine learning (ML) based method, MWCNN, shows promising results across different noise values while showing impressive PSNR (Peak Signal-to-Noise Ratio) and SSIM (Structural Similarity Index Measure) values in the order of 55.98 and 0.999 respectively. It is also observed that the ML models show poor results when the training data is not sufficient. Therefore, unlike conventional denoising methodologies, for desirable results, we need substantially diverse training data for satisfactory results. However, our results show that DL-based denoising methods perform better than widely used conventional methodologies, and open up many possibilities for research requiring denoising as a precursor for several plasma imaging-based diagnostics.**

I. INTRODUCTION

Nuclear fusion is an eye-catching concept for future energy generation strategies, with an almost unlimited amount of raw material available [1] [2]. Tokamak, a device for magnetic confinement of the high-temperature plasma, is one of the promising architectures which assists in realizing the potential of nuclear fusion [3] [4]. Sustained tokamak plasma operations require information on the plasma shape and the plasma interior. This information is directly related to plasma stability and equilibrium. The imaging diagnostics, a class of the tokamak plasma diagnostics, offer the capability to have detailed monitoring of plasma shape, emission profile shapes, and the interior [5] [6] [7] [8]. Images of plasma corresponding to various emission profiles are captured across different wavelengths addressing different aspects of the plasma condition. These images are then employed for the tomographic reconstructions for the recovery of the plasma instabilities as well as any modification in the plasma emission profiles [9]. Such critical information can serve as possible feedback for prolonged plasma operations.

The imaging diagnostic consists of an efficient emission light collection system, optical assembly of lenses and mirrors, or optical fiber bundles, coupled with a sophisticated detector system. The detector systems, which operates at different wavelength, converts the plasma emission light into detectable electrical signals. These electrical signals are later processed by a capable electronic architecture, resulting in the final image output [10]. These complete imaging diagnostic systems are operated in a very complex environment having high and time-varying magnetic/ electric field, with substantial heating due to operations, and energetic particle interaction. Such conditions introduce noises within the diagnostic data received from imaging diagnostics (ID) [10] [11]. The noises observed in the ID data are principally undesired brightness variations, purely unrelated to the plasma emissions. Therefore, a prerequisite for any scientific analysis, tomographic reconstruction, is to subject the ID data to a robust "denoising treatment"[doi: 10.1186/s42492-019-0016-7, https://doi.org /10.1016/j.inffus. 2019.09.003]. Denosing of the ID images, before any tomographic reconstruction, is generally carried out by singular value decomposition (SVD). By removing inessential information associated with smaller singular values, SVD simultaneously serves as both a denoising tool and a means of dimension compression (DC). DC plays a crucial role in accelerating the implementation of tomographic reconstruction and mitigating computationally expensive calculations. Although the SVD works well for most occasions, the smaller singular values also hold some valuable particular information about the plasma emission observed by the detector. Therefore, ignoring the smaller singular values can result in the loss of that specific information. This article proposes a new approach where the images are denoised prior to the application of SVD. This allows SVD to focus primarily on dimension compression while restricting the information loss when considering only the higher singular values.

There are a wide range of image-denoising procedures like filtering out the noise, or newly introduced Deep learning (DL) based methods[Remote Sens. 2019, 11, 1910; doi:10.3390/rs11161910, DOI: 10.1109/I-CICIS52592.2021.9694140 https:// doi.org /10.1016/j.inffus. 2019. 09. 003]. [12] [13] [14], However, to date, there has been limited exploration of their potential use in the realm of tokamak imaging diagnostics. The article presents a careful review of synthetic tokamak ID image denoising methodologies for a wide variety of experimental situations, namely, different types of noise, noise magnitude, amount of training data required for accurate denoising, emission

profile dependency, etc. Like filtering out the noise, or newly introduced Deep learning (DL) based methods. Off late several efficient Machine Learning based image-denoising approaches and procedures are available [12] [13] [14]. The article identifies the most efficient methods for image denoising processes for tokamak ID, in general, or for a particular noise type. Thereafter the selected image denoising process is applied before the SVD and the performance is evaluated, to understand the effect of denoising over SVD efficiency and subsequent dimension compression. The experimental setup for this study is presented in section II, which includes, viewing geometry, synthetic image generations, training, and testing data sets categorization. The proposed Methods for this paper are mentioned in section III. The results and discussion for the comparative study of different image denoising processes in this section IV/. The ablation study is elaborated in section V. Comparison of SVD performance with and without image denoising is presented in section VI. This is followed by the summary, section VII.

II. EXPERIMENTAL SETUP

The experimental setup for investigating the denoising of tokamak imaging diagnostics includes generating the synthetic image,defining the training and testing datasets, and identifying the questions which motivates the creation of specific types of training and testing datasets.

A. Synthetic image generation

The synthetic images (SI) for tokamak plasma diagnostics is the first requirement for this study. The SI comprises two major components: the line-integrated emission information along the line of sight for the camera pixels and the noise within the image.

A higher aspect ratio ($\tilde{3}$) tokamak plasma is considered with circular poloidal limiter, up-down symmetry, configuration. The plasma core temperature is sub keV and the electron density is of the order of $10^{19} m^{-3}$. A fast frame rate camera, for which the SI is created, is stationed at the plasma mid-plane viewing the plasma tangentially, see figure 1. The camera has 128x128 active pixels, covering a total of 1.25 inches x 1.25 inches of the sensor area. The light collection from the plasma to the camera sensor plane is performed by an optical assembly, avoiding any issue with the dead space of the optical fiber bundles. The visible emission type of profile is considered for this study, however, the results can be extended to other emission profiles like the soft X-ray, which is Gaussian in nature. Different types of noises appear within the SI images, however, Gaussian, Poisson and salt-and-pepper noises are considered here for which the denoising is carried out. The quantity and type of noise introduced to the SI can be adjusted to align with various scientific objectives. A comprehensive guide to constructing the SI, which includes adding noise to the line-integrated emissions can be found in the literature [16].

B. Denoising approaches

Numerous image denoising methods are currently utilized, and advances in deep learning (DL), machine learning (ML), and artificial intelligence (AI) have created a new realm in
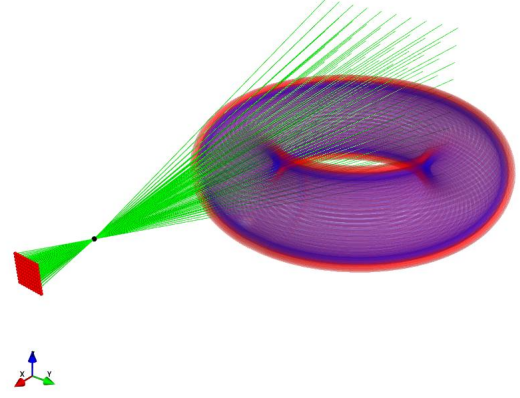

Fig. 1: Experiment setup for generating plasma image

which image denoising can be accomplished more effectively. These novel techniques can be classified into two primary categories, supervised learning and unsupervised learning. Supervised learning relies on a ground truth dataset or a denoised image for performance comparison and efficiency enhancement, while unsupervised learning necessitates a domain expert to evaluate the quality of denoising. The study presented in this article focuses on supervised learning techniques and traditional image denoising strategies. The traditional denoising methods encompass the median filter, Gaussian filter, Bilateral filter, Wiener filter, Block-matching 3D filter(BM3D) and Non-Local Means filter (NLM), while the DL approaches include DnCNN, REDNet, CBDNet, PRIDNet, and MWCNN. A brief description of the methods are provided below:

1) Median filter: In the median filter technique, the intensity value of each pixel is replaced with the median value of its surrounding pixels within a filter window. This window typically has a square shape, such as 3x3 or 4x4 pixels, and includes the pixel for which the intensity value is being replaced. The size of the window is selected based on user assessment. The present study considers a square window of 3x3 pixels surrounding the particular pixel [17].

2) Gaussian filter: A Gaussian kernel is considered and convolved with the sliding window for each pixel, and the center value of the window is replaced with the result of the convolution. The Gaussian kernel is normalized so that its integral evaluates to 1, ensuring that the overall brightness of the image is not changed [18].

3) Bilateral filter: Two Gaussian functions are employed, one for coordinate space (typically a 7x7 kernel) and another for color space (the difference in intensity values from the centre pixel to each pixel in the window). Both kernels are multiplied with a sliding window. The results are added and normalized [19].

4) Wiener: The Wiener filter is a signal processing filter that is used to estimate a preferred or target random process by linear time-invariant (LTI) filtering a measured noisy process with known stationary signal and noise spectra

and additive noise. The Wiener filter minimizes the mean square error between the approximate and favoured random processes [20].

5) BM3D: Block-matching and 3D filtering (BM3D) is a 3-D block-matching method that is mainly used for image denoising. It is one of the non-local means of methodology extensions. In BM3D, there are two cascades: a hard thresholding stage and a Wiener filter stage, both of which involve aggregation, grouping, and collaborative filtering. This algorithm is predicated on an enhanced representation at the transformation location [21].

6) NLM: Non-local means is an image processing method used for image denoising. Non-local means filtering computes the average of all pixels within the image, weighted by their similarity to the target pixel. When compared to local mean methodologies, this outcome in much greater post-filtering clarity and less loss of quality images [22].

7) PRIDNet: There are three stages in this network. The channel's initial stage of noise estimation implements a channel attention mechanism to determine the significance of input noise. Second, multi-scale features are extracted using pyramid pooling during the multi-scale denoising stage. Third, kernel selection is used in the feature fusion stage to combine multi-scale features [23].

8) MWCNN: With the help of this network, the trade-off between computational speed and receptive field size will be improved. In the modified U-Net architecture, wavelet transform is used to condense the size of feature maps in the contracting subnetwork. In addition, a second convolutional layer is applied to feature maps to reduce the number of channels. The high-resolution feature maps are then recreated in the expanding subnetwork using the inverse wavelet transform [24].

9) REDNet: This network, which is an encoding decoding framework with symmetric convolutional deconvolutional layers, presents a very deep fully convolutional auto-encoder network for image restoration in this paper. In other words, the network learns end-to-end mappings from noisy images to the original ones by layering convolution and deconvolution operators. Convolutional layers abstract image data while cleaning up errors. Deconvolutional layers are capable of retrieving image details and feature maps which takes some time [25].

10) DnCNN: This network recognizes the deep learning architecture, regularisation techniques, and learning algorithms for image denoising. To speed up the training process, batch normalization and residual learning are also used. Furthermore, this network can manage Gaussian denoising with unidentified noise sigma levels [26].

11) CBDNet: To provide an interactive strategy for conveniently correcting denoising results, a noise prediction subnetwork with asymmetric learning to suppress the underestimation of noise level is integrated into CBDNet [27].

C. Denoising evaluation

The evaluation of the denoised images is an important requirement. As the SI can be generated without the noise too therefore the extent of the denoising can be realized. The synthetic image without the noise is referred to as a ground truth image (GTI) and all the denoised images are compared with the GTI for evaluation. The Peak Signal-to-Noise Ratio (PSNR) and Structural Similarity Index Measure (SSIM) are the two parameters over which the evaluation has been carried out.

1) Peak Signal-to-Noise Ratio (PSNR) : Metric for the ratio between the maximum possible power of the signal and the power of corrupting noise that affects the fidelity of its representation. Because many signals have a wide dynamic range, PSNR is usually expressed as a logarithmic quantity using the decibel scale. PSNR is commonly used to quantify reconstruction quality for images and video subject to lossy compression.

$$PSNR = 10 \log_{10} \left(\frac{255}{RMSE} \right)$$

Here, RMSE is Root Mean Squared Error.

2) Structural Similarity Index Measure (SSIM) : This metric measures the perceptual difference between the two images.

$$SSIM = \frac{(2\mu_x \mu_y)(2\sigma_{xy} + c_2)}{(\mu_x^2 + \mu_y^2)(\sigma_x + \sigma_y)}$$

Here, μ_x and μ_y are the mean intensity values of images x and y, σ_x^2 is the variance of x, σ_y^2 is the variance of y and σ_{xy}^2 is covariance of x and y.

III. RESULTS AND DISCUSSION

The denoising performance of the traditional and the other DL-based methods is evaluated and the best denoising method is then applied before the SVD to explore the effectiveness of the SVD. In the first section, the results from the traditional and DL methods are compared.

A. Traditional Vs DL based

The SI considered is with the 128x128 pixels with a noise configuration of all Gaussian, Poisson, and Salt & Pepper with noise level 40, which is then subjected to all the denoising strategies discussed in the previous section. The results are presented in figure 2 and the quantitative evaluation is given in table – 1. It is very much evident that the traditional methods do not perform significantly in comparison with the DL methods. The PSNR and SSIM values, shown in table –1, exhibit the poor performance quantitatively, as the traditional methods achieve significantly lower values, in the range of 17 to 22. It is concluded that for the tokamak imaging diagnostic DL based denoising methods are a better choice.

B. Comparison of DL-based denoising

Referring to the figure - 2, Although the DL-based methods perform well for denoising tokamak images not all of them exhibit good performance. Methods like REDNet or DnCNN perform poorly even poor than some of the traditional methods. These results suggest a strong review
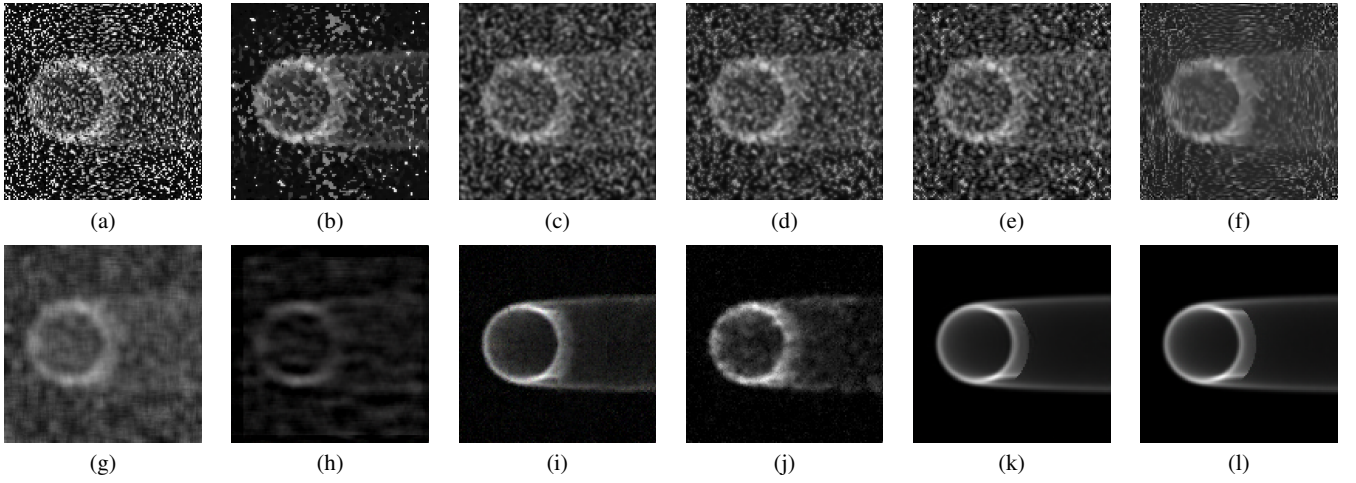
Fig. 2: Image denoising result of *Test Dataset 3* with noise level 40. (a) Noisy (b) Median (c) Gaussian (d) Bilateral (e) Wiener (f) BM3D (g) NLM (h) REDNet (i) CBDNet (j) DnCNN (k) PRIDNet (l) MWCNN.

TABLE 1: Average PSNR(dB)/SSIM results of the competing methods for image denoising with noise levels σ = 40 on *test datasets 4*. Red and Blue color indicates the best and second best performance accordingly.

σ	Medain	Guassian	Bilateral	Wiener	BM3D	NLM	REDNet	CBDNet	DnCNN	PRIDNet	MWCNN
40	15.20 / 0.1001	12.87 / 0.0902	12.94 / 0.0889	12.43 / 0.0845	13.41 / 0.0949	13.28 / 0.1000	20.02 / 0.1967	29.64 / 0.6982	27.93 / 0.2135	51.17 / 0.9965	51.78 / 0.9983

of the DL-based method for the identification of the best method for denoising tokamak images. The review is carried out mainly to understand how the denoising capability of the given methods has for individual noise or the mixture of them. How the capability depends on the training data sets too.

To answer these questions special training and testing data sets are created. Four training data sets (each training dataset contains 50 images (128x128)) are created with the following characteristics.

1) Images with all noises, Gaussian noise, Poisson noise, and Salt-pepper noise separately with different sigma varying from 10 to 80, with an interval of 10.
2) Consists of images with all Gaussian noise, Poisson noise, and Salt-pepper noise mixed with varying sigma from 10 to 80 with an interval of 10.
3) Consists of images with all Gaussian noise, Poisson noise, and Salt-pepper noise separately varying noise sigma from 10 to 30, with an interval of 10.
4) Consists of images with all Gaussian noise, Poisson noise, and Salt-pepper noise mixed with sigma equal to 40.

Five testing data sets (each training dataset contains 10 images (128x128)) are created with the following characteristics.

1) Images with only Gaussian noise.
2) Images with only Poisson noise.
3) Images with only Salt-pepper noise.
4) Images with mixed Gaussian noise, Poisson noise, and Salt-pepper noise.
5) Images with all three noises separately with noise sigma 60 to 80, at an interval of 10.

Evaluating the individual denoising capability all DL models are trained with the first training dataset and tested them

testing datasets 1,2, and 3 at noise levels, σ=20, 40, 60, and 80. The results are shown in table -2. The MWCNN and PRIDNet models achieve the best and second-best PSNR/SSIM on all three test datasets. The difference between the two increases with the increase in noise and peaks at σ = 80. The PRIDNet performance deteriorates significantly with high salt and pepper noise. The MWCNN seems to be the best DL method for individual noise denoising.

The performance with the integrated noise is carried out while training the models on the 2nd training data set and testing on the 4th testing data set at noise levels, i.e., σ=20, 40, 60, and 80. The results are presented in table -3. It is clear that with lower noise (σ = 20) the PRIDNet performs well for the integrated noises, whereas with the rising noise levels, MWCNN performs significantly better. PRIDNet performance deteriorate with increasing noise, however, it is still better than the other DL-based denoising models.

The distribution of the noises in any image can be of any random configuration for any experimental situation. Some identified noses information is known like Gaussian noise etc, however not all The DL models capability to denoise the integrated noises images while trained on individual noisy images is something of interest as this increases the scope of the DL models. Models are trained on individual noises, first training data set, and tested integrated noises, 4th test data set at noise level σ = 40. The results are shown in table -4 and fig 3. The MWCNN and the PRIDNet perform well with MWCNN achieving the best PSNR and SSIM values. While in the inverse situation, trained on integrated noise data set 4 and tested on data set 1,2,3 the results are totally surprising, see table -5 and fig 4. The PRIDNet performs far better than the MWCNN even with the higher salt and pepper noise.

TABLE 2: Average PSNR(dB)/SSIM results of the competing methods for image denoising with noise levels σ = 20, 40, 60 and 80 on *test datasets 1, 2 and 3*. Red and Blue color indicates the best and second best performance accordingly.

Datasets	σ	Medain	Guassian	Bilateral	Wiener	BM3D	NLM	REDNet	CBDNet	DnCNN	PRIDNet	MWCNN
Test Dataset 1	20	31.34 / 0.4195	30.95 / 0.4216	30.94 / 0.4213	31.11 / 0.4232	30.87 / 0.4106	27.63 / 0.3617	24.16 / 0.6625	34.67 / 0.6383	39.60 / 0.4592	53.07 / 0.9985	56.53 / 0.9991
	40	29.65 / 0.3922	29.37 / 0.4026	29.36 / 0.4027	29.48 / 0.4016	29.36 / 0.4005	26.78 / 0.3530	24.41 / 0.5712	33.91 / 0.8982	38.69 / 0.4227	52.62 / 0.9982	55.88 / 0.9991
	60	28.48 / 0.3724	28.25 / 0.3860	28.25 / 0.3863	28.35 / 0.3832	28.27 / 0.3948	26.10 / 0.3447	24.66 / 0.5240	33.22 / 0.6832	36.47 / 0.3723	51.18 / 0.9973	53.40 / 0.9990
	80	26.57 / 0.3465	26.44 / 0.3633	26.44 / 0.3639	26.50 / 0.3598	26.47 / 0.3862	24.88 / 0.3315	24.81 / 0.4921	33.07 / 0.8068	33.60 / 0.3601	51.94 / 0.9961	55.28 / 0.9989
Test Dataset 2	20	30.71 / 0.4122	30.34 / 0.4206	30.33 / 0.4202	30.48 / 0.4227	30.31 / 0.4074	27.34 / 0.3594	24.22 / 0.6297	35.47 / 0.8606	41.42 / 0.4728	53.53 / 0.9986	57.13 / 0.9991
	40	29.28 / 0.3951	29.00 / 0.4053	28.99 / 0.4053	29.11 / 0.4054	28.98 / 0.3989	26.55 / 0.3524	24.55 / 0.5350	34.25 / 0.8749	38.40 / 0.4181	52.49 / 0.9982	56.01 / 0.9991
	60	26.89 / 0.3714	26.72 / 0.3863	26.72 / 0.3864	26.79 / 0.3848	26.74 / 0.3873	25.83 / 0.3411	24.84 / 0.4911	31.70 / 0.6956	32.86 / 0.3797	52.40 / 0.9980	56.36 / 0.9990
	80	26.97 / 0.3609	26.78 / 0.3771	26.78 / 0.3775	26.86 / 0.3742	26.75 / 0.3856	25.09 / 0.3381	24.77 / 0.4801	29.34 / 0.6001	28.72 / 0.3613	52.21 / 0.9969	54.99 / 0.9989
Test Dataset 3	20	23.12 / 0.2005	18.72 / 0.1433	18.86 / 0.1435	17.92 / 0.1354	21.94 / 0.1814	19.79 / 0.1570	22.44 / 0.2879	26.27 / 0.4937	27.68 / 0.2105	39.95 / 0.9833	42.12 / 0.9894
	40	16.08 / 0.1023	13.82 / 0.0900	13.85 / 0.0884	13.09 / 0.0837	14.24 / 0.0951	14.27 / 0.1035	19.75 / 0.2104	22.48 / 0.3920	24.73 / 0.1462	38.65 / 0.9715	43.40 / 0.9926
	60	11.05 / 0.0519	10.66 / 0.0571	10.58 / 0.0545	9.99 / 0.0520	10.25 / 0.0501	11.10 / 0.0705	17.10 / 0.1525	20.57 / 0.2495	19.27 / 0.0716	29.27 / 0.9360	43.23 / 0.9931
	80	8.64 / 0.0205	8.98 / 0.0200	8.86 / 0.0197	8.42 / 0.0195	8.48 / 0.0162	9.29 / 0.0216	15.25 / 0.0883	17.97 / 0.1367	15.53 / 0.0260	23.98 / 0.5411	42.11 / 0.9935

TABLE 3: Average PSNR(dB)/SSIM results of the competing methods for image denoising with noise levels σ = 20, 40, 60 and 80 on *test datasets 4*. Red and Blue color indicates the best and second best performance accordingly.

Datasets	σ	Medain	Guassian	Bilateral	Wiener	BM3D	NLM	REDNet	CBDNet	DnCNN	PRIDNet	MWCNN
Test Dataset 4	20	22.24 / 0.1812	17.86 / 0.1420	18.04 / 0.1422	17.34 / 0.1347	20.56 / 0.1823	18.51 / 0.1531	21.04 / 0.2604	31.29 / 0.5964	30.56 / 0.5626	51.17 / 0.9969	46.83 / 0.9982
	40	15.20 / 0.1001	12.87 / 0.0902	12.94 / 0.0889	12.43 / 0.0845	13.41 / 0.0949	13.28 / 0.1000	20.02 / 0.1967	29.64 / 0.6982	27.93 / 0.2135	51.17 / 0.9965	51.78 / 0.9983
	60	10.76 / 0.0527	9.98 / 0.0541	9.96 / 0.0524	9.58 / 0.0500	9.88 / 0.0480	10.27 / 0.0617	18.53 / 0.1237	28.46 / 0.5433	23.06 / 0.1139	42.35 / 0.9897	51.74 / 0.9982
	80	8.29 / 0.0212	8.58 / 0.0209	8.49 / 0.0199	8.17 / 0.0190	8.27 / 0.0161	8.82 / 0.0270	17.40 / 0.1058	26.44 / 0.5705	20.53 / 0.0546	38.44 / 0.9828	41.78 / 0.9970

TABLE 4: Average PSNR(dB)/SSIM results of the competing methods for trained on '*first training data set*' and tested on *test dataset 4*. Red and Blue color indicates the best and second best performance accordingly.

Datasets	REDNet	CBDNet	DnCNN	PRIDNet	MWCNN
Test Dataset 4	19.48 / 0.2089	22.93 / 0.4240	23.23 / 0.1328	34.89 / 0.9072	39.26 / 0.9912

TABLE 5: Average PSNR(dB)/SSIM results of the competing methods for trained on '*integrated noise data set 4*' and tested on *test datasets 1,2 and 3*. Red and Blue color indicates the best and second best performance accordingly.

Datasets	REDNet	CBDNet	DnCNN	PRIDNet	MWCNN
Test Dataset 1	21.20 / 0.5995	28.94 / 0.7924	31.06 / 0.3773	32.13 / 0.9182	18.98 / 0.4248
Test Dataset 2	21.28 / 0.5925	27.85 / 0.7552	29.73 / 0.3813	31.63 / 0.8882	19.12 / 0.4383
Test Dataset 3	20.02 / 0.1958	24.87 / 0.3212	26.31 / 0.2086	45.05 / 0.9928	36.80 / 0.9955

The dependence of the noise magnitude in the training is explored. The DL models are trained on the lower noise values, σ = 10 to 30, and tested on the higher noise, 5th testing data set. The results are given in table 6. Overall PSNR and SSIM values are reduced across DL models. PRIDNet and MWCNN both perform well, but PRIDNet PSNR is 6.5 dB more than the MWCNN therefore PRIDNet will be considered for this kind of situation.

TABLE 6: Average PSNR(dB)/SSIM results of the competing methods for trained on '*third training data set*' and tested on *test dataset 5*. Red and Blue color indicates the best and second best performance accordingly.

Datasets	REDNet	CBDNet	DnCNN	PRIDNet	MWCNN
Test Dataset 5	23.64 / 0.3784	25.12 / 0 .3924	25.76 / 0.2616	38.87 / 0.7434	32.36 / 0.7778

Denosing performance dependency over the volume of the training data is also important. The DL models are trained over different volumes of the first data set with noise level σ = 40 and tested on the 1st testing data set, see table -7 and fig 5 and 6. The result shows that PRIDNet requires a lower

training dataset however at a higher volume of training data the performance does not change much. Whereas for MWCNN the performance increases with the increase in the training data volume. Surprisingly for other DL methods, the PSNR/ SSIM does not show a clear trend. The mentioned investigations strongly suggest that the MWCNN is the best DL model within the DL model considered.

TABLE 7: Average PSNR(dB)/SSIM results of the competing methods for trained on '*first training data set*' and tested on *Test datasets 1* with noise level equal to 40. Red and Blue color indicates the best and second best performance accordingly.

DL-methods	50	100	150	200	250
REDNet	24.41 / 0.5712	23.38 / 0.5504	24.94 / 0.5631	23.94 / 0.5821	24.21 / 0.5364
DnCNN	38.69 / 0.4227	38.29 / 0.4152	38.11 / 0.4025	28.94 / 0.3549	43.81 / 0.4571
CBDNet	33.91 / 0.8982	38.06 / 0.7360	37.12 / 0.7663	38.94 / 0.7937	37.94 / 0.7292
PRIDNet	52.62 / 0.9982	58.84 / 0.9991	55.97 / 0.9992	52.66 / 0.9984	55.66 / 0.9988
MWCNN	55.88 / 0.9991	53.92 / 0.9991	58.39 / 0.9995	59.77 / 0.9995	59.70 / 0.9995

IV. ABLATION STUDY

According to the experimental findings, deep learning offers a higher PSNR than the traditional method for removing noise from images. MWCNN is gives overall best results. MWCNN architecture is shown in Fig. 11. Designing the CNN block after each level. of DWT is the key to the MWCNN architecture. The subband images are inputs into each CNN block, which is a 4-layer FCN without pooling. The ablation study's objective is to thoroughly understand the model's performance by examining the effects of alteration of different components or hyper-parameters. With the alteration of various components of a model, a change in performance is observed. This technique can detect any potential decline in the model's performance, which can be fixed by updating the network. Therefore, we train the MWCNN model several times by altering CNN block numbers, filer sizes, and changing the number of filters. The "Results of the ablation study" subsection contains the research outcome.
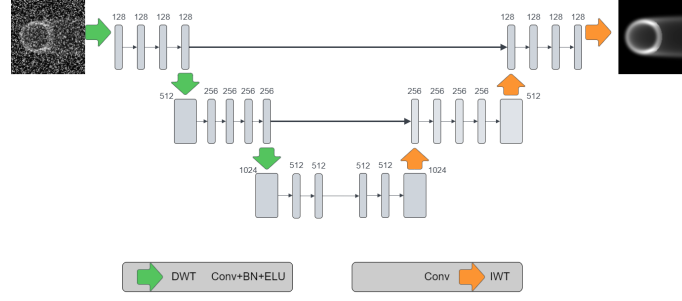
Fig. 12: MWCNN architecture

A. Results of the ablation study

All the experiments are performed on Train Dataset 1 and tested on Test Dataset 1. The entire base CNN architecture is modified, and the outcomes are validated. We display the PSNR/SSIM for evaluation for each case study.

Case study 1: Changing CNN block number: In this case study, the number of convolutional neural networks is changed. Initially, we start with 4 CNN blocks. Table X shows the performance of different configurations of the model architecture with the PSNR and SSIM. The best performance is achieved by configuration 3 (TABLE VII) with a PSNR of 58.81 and SSIM of 0.9995. Configuration 3 consists of 2 CNN blocks. This configuration was selected for the rest of the ablation case studies.

TABLE VII: Changing CNN block number

Configuration no.	No. of CNN block	PSNR/SSIM	Finding
1	4	54.35 / 0.9991	Modest accuracy
2	3	45.47 / 0.9957	Lowest accuracy
3	2	58.81 / 0.9995	Highest accuracy
4	1	54.59 / 0.9990	Modest accuracy

Case study 2: Changing filter size: To evaluate performance in this case study, we experimented with various kernel sizes, including 3x3, 2x2, and 5x5. It has been found that altering the filter size has little impact on overall performance(TABLE VIII). However, the highest PSNR of 58.81 is achieved when employing the kernel size 3x3. Filter 5x5 had the second-highest PSNR of 57.67. Here, configuration 1 gives the best PSNR and SSIM, so this configuration is selected for further ablation study.

TABLE VIII: Changing filter size

Configuration no.	Filter size	PSNR/SSIM	Finding
1	2 x 2	58.81 / 0.9995	Highest accuracy
2	3 x 3	55.30 / 0.9990	Lowest accuracy
3	5 x 5	57.67 / 0.9994	Accuracy improved

Case Study 3: Changing the number of filters: Initially, we started with 64-128-512-512-512-128-256-64-128-3 number of kernels for down scaling and up scaling CNN. Then we reduced the feature by 32-64-256-256-256-64-128-32-64-3, and no improvement in performance is found. So

we increase the kernels by 128-256-1024-1024-1024-256-512-128-256-3, but still no improvement in performance(TABLE IX). So we selected configuration 1 for further ablation study.

TABLE IX: Changing the number of filters

Configuration no.	No. of kernel	PSNR/SSIM	Finding
1	64-128-512-512-512-128-256-64-128-3	58.81 / 0.9995	Highest accuracy
2	32-64-256-256-256-64-128-32-64-3	58.35 / 0.9994	Modest accuracy
3	128-256-1024-1024-1024-256-512-128-256-3	57.04 / 0.9994	Lowest accuracy

Case study 4: Changing the activation function: Selecting the best activation function is becoming a pertinent research question because different activation functions can affect how well a neural network model performs. We experiment with four activation functions: ReLU, Leaky ReLU, Thresholded ReLU, and Exponential Linear Units (ELUs). ELU performs best with a PSNR of 58.99 (TABLE X). For additional ablation studies, this activation function was chosen.

TABLE X: Changing the activation function

Configuration no.	Activation function	PSNR/SSIM	Finding
1	Relu	58.81 / 0.9995	Near Highest accuracy
2	ELU	58.99 / 0.9994	Highest accuracy
3	LeakyRelu	50.88 / 0.9979	Lowest accuracy
4	ThresholdedReLU	55.03 / 0.9990	Modest accuracy

Case study 5: Changing optimizer: To find the ideal optimizer, experiments were done with a variety of optimizers, including Adam, Nadam, Adamax, and RMSprop.The learning rate in this instance was set to 0.0009. With the RMSprop optimizer, the highest test PSNR was recorded, coming in at 59.50(TABLE XI). We decide to continue our study of ablation with the RMSprop optimizer.

TABLE XI: Changing optimize

Configuration no.	Optimizer	PSNR/SSIM	Finding
1	Adam	58.99 / 0.9994	Near Highest accuracy
2	Nadam	46.81 / 0.9966	Lowest accuracy
3	Adamax	58.76 / 0.9994	Modest accuracy
4	RMSprop	59.50 / 0.9995	Highest accuracy

Case study 6: Changing learning rate: Different learning rates of 0.0001, 0.0005, 0.0009, and 0.0015 were tested in the experiment. With a learning rate of 0.0005 and the RMSprop

optimizer, the best test PSNR of 63.45 (TABLE XII) was obtained.

TABLE XII: Changing learning rate

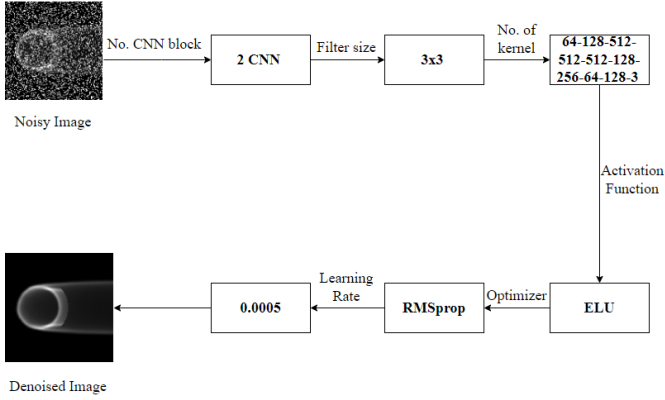| Configuration no.	Learning rate	PSNR/SSIM	Finding
1	0.0009	59.50 / 0.9995	Modest accuracy
2	0.0001	58.25 / 0.9994	Lowest accuracy
3	0.0005	63.45 / 0.9997	Highest accuracy
4	0.0015	60.69 / 0.9995	Modest accuracy

B. Conclusion of Ablation Study

Fig. 13: Ablation study on the image from *Test Dataset 3*.

Here, we conducted ablation study on MWCNN network. According to our results, when we use 2 CNN blocks with filter size 3x3 and no. of filter 64-128-512-512-512-128-256-64-128-3 alongside ELU activation function, RMSprop optimizer and learning rate of 0.0005, it gives the best performance.

V. MWCNN APPLICATION TO SVD

Denosing of the SI before SVD is the main goal of the article. The noisy image is considered for all the noises with 10 to 80 noise levels. The image is reconstructed back by SVD considering 10, 25, and 40 singular values having with and without prior denoising with MWCNN. The results are shown in figure 7. One can see that without denoising the image is not clear at all even when considering 40 singular values. The SSIM for 40 singular value is at 0.2169. Whereas with prior denoising, an SSIM of 0.9531 is achieved with just the first 10 singular values. The SSIM increased to 0.9991 at 40 singular values. Prior denoising helps the SVD performance. Therefore, it can be said that prior denoising improves the efficiency of the SVD.
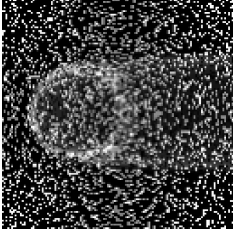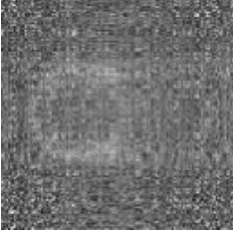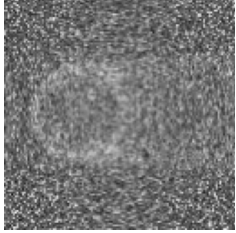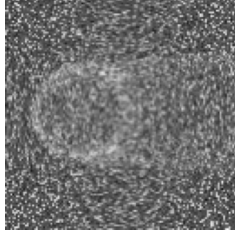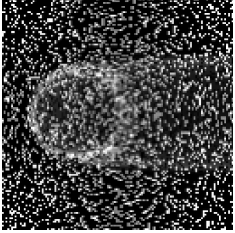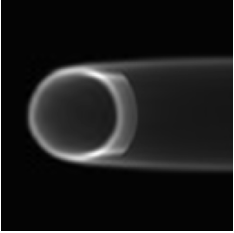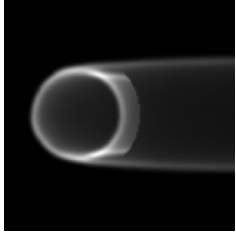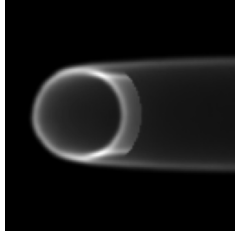
Approaches	Noisy Image	first 10 singular values	first 25 singular values	first 40 singular values
SVD	0.0513	0.2145	0.2166	0.2169
MWCNN + SVD	0.0513	0.9531	0.9823	0.9991

Fig. 7: Comparison of SVD with MWCNN+SVD. The SSIM are shown below every images.

VI. Summary

The article demonstrates a robust algorithm for estimations of synthesis images having tangential viewing 2D imaging diagnostic for circular tokamak plasma cross-section. A critical review of the available image-denoising algorithms, six traditional filtering techniques, and five different deep-learning techniques are performed. The performance evaluation is conducted on the bases of PSNR values (higher values indicate good results), as the ground-truth images are available. The experimental findings reveal that the deep learning approach offers a higher PSNR, typical PSNR values, than the traditional method, typical PSNR values, for removing noise from images. The MWCNN performs the best for individual denoising, and individual type of noise removal, as well as for integrated noise, integrated noise including all possible noise, removal (PSNR values). Such performance is observed when trained over integrated noisy images. However, MWCNN, when trained on the trained over individual noise, it is capable of image denoising by having integrated noise, PSNR values. The MWCNN denoise individual Gaussian noise image while trained over different train sizes. The study also observes that the PRIDNet performs the best for denoising individual noise while trained over integrated noise, PSNR values. The MWCNN is applied before the SVD for denoising as found to be the best for the denoising review. Prior denoising by the MWCNN method shows substantial improvement in the SVD performance, PSNR values. The results suggest that the proposed method significantly improves SVD performance.

References

[1] Strachan, J. D., et al. "High-temperature plasmas in a tokamak fusion test reactor." Physical review letters 58.10 (1987): 1004.

[2] Strachan, J. D. "Studies of global energy confinement in TFTR super-shots." Nuclear fusion 34.7 (1994): 1017.

[3] Keilhacker, M., et al. "High fusion performance from deuterium-tritium plasmas in JET." Nuclear Fusion 39.2 (1999): 209.

[4] Budny, R. V., et al. "Core fusion power gain and alpha heating in JET, TFTR, and ITER." Nuclear Fusion 56.5 (2016): 056002.

[5] Equipe, T. F. R. "Tokamak plasma diagnostics." Nuclear Fusion 18.5 (1978): 647.

[6] Nagayama, Y. "Tomography on tokamak fusion test reactor." Review of scientific instruments 65.11 (1994): 3415-3422.

[7] Von Goeler, S., et al. "Tangential imaging for fluctuation studies." Review of scientific instruments 61.10 (1990): 3055-3057.

[8] Nilson, D. G., et al. "A tangentially viewing vacuum ultraviolet TV system for the DIII–D divertor." Review of scientific instruments 70.1 (1999): 738-741.

[9] Ohdachi, S., et al. "Magnetic islands observed by a fast-framing tangentially viewing soft x-ray camera on LHD and TEXTOR." Plasma Science and Technology 8.1 (2006): 45.

[10] Shu, Shuangbao, et al. "Plasma image edge detection based on the visible camera in the EAST device." SpringerPlus 5.1 (2016): 1-13.

[11] Ming, Tingfeng, et al. "Investigation of the noise effect on tomographic reconstructions for a tangentially viewing vacuum ultraviolet imaging diagnostic." Plasma and Fusion Research 6 (2011): 2406120-2406120.

[12] Tian, Chunwei, et al. "Deep learning on image denoising: An overview." Neural Networks 131 (2020): 251-275.

[13] D. Liu, B. Wen, J. Jiao, X. Liu, Z. Wang and T. S. Huang, "Connecting Image Denoising and High-Level Vision Tasks via Deep Learning," in IEEE Transactions on Image Processing, vol. 29, pp. 3695-3706, 2020, doi: 10.1109/TIP.2020.2964518.

[14] Zhang, Fu, et al. "Image denoising method based on a deep convolution neural network." IET Image Processing 12.4 (2018): 485-493.

[15] Y. Nagayama, M. Yamada, W. Park, E. Fredrickson, A. Janos, K. McGuire, and G. Taylor, "Tomography of full sawtooth crashes on the tokamak fusion test reactor," Physics of Plasmas, vol. 3, no. 5, pp. 1647–1655, 1996.

[16] K. Delwadia, D. Bhatt, S. Purohit, and B. Chaudhury, "Parallel algorithm for synthetic image generation with application to tokamak plasma diagnostics," Concurrency and Computation: Practice and Experience, vol. 34, no. 24, p. e7217, 2022.

[17] T. Huang, G. Yang, and G. Tang, "A fast two-dimensional median filtering algorithm," IEEE transactions on acoustics, speech, and signal processing, vol. 27, no. 1, pp. 13–18, 1979.

[18] A. Buades, B. Coll, and J.-M. Morel, "A review of image denoising algorithms, with a new one," Multiscale modeling & simulation, vol. 4, no. 2, pp. 490–530, 2005.

[19] S. Paris, P. Kornprobst, J. Tumblin, F. Durand et al., "Bilateral filtering: Theory and applications," Foundations and Trends® in Computer Graphics and Vision, vol. 4, no. 1, pp. 1–73, 2009.

[20] M. Kazubek, "Wavelet domain image denoising by thresholding and wiener filtering," IEEE Signal Processing Letters, vol. 10, no. 11, pp. 324–326, 2003.

[21] K. Dabov, A. Foi, V. Katkovnik, and K. Egiazarian, "Image denoising by

sparse 3-d transform-domain collaborative filtering," *IEEE Transactions on image processing*, vol. 16, no. 8, pp. 2080–2095, 2007.

[22] A. Buades, B. Coll, and J.-M. Morel, "A non-local algorithm for image denoising," in *2005 IEEE computer society conference on computer vision and pattern recognition (CVPR'05)*, vol. 2.   Ieee, 2005, pp. 60–65.

[23] Y. Zhao, Z. Jiang, A. Men, and G. Ju, "Pyramid real image denoising network," in *2019 IEEE Visual Communications and Image Processing (VCIP)*.   IEEE, 2019, pp. 1–4.

[24] P. Liu, H. Zhang, K. Zhang, L. Lin, and W. Zuo, "Multi-level wavelet-cnn for image restoration," in *Proceedings of the IEEE conference on computer vision and pattern recognition workshops*, 2018, pp. 773–782.

[25] X.-J. Mao, C. Shen, and Y.-B. Yang, "Image restoration using convolutional auto-encoders with symmetric skip connections," *arXiv preprint arXiv:1606.08921*, 2016.

[26] K. Zhang, W. Zuo, Y. Chen, D. Meng, and L. Zhang, "Beyond a gaussian denoiser: Residual learning of deep cnn for image denoising," *IEEE transactions on image processing*, vol. 26, no. 7, pp. 3142–3155, 2017.

[27] S. Guo, Z. Yan, K. Zhang, W. Zuo, and L. Zhang, "Toward convolutional blind denoising of real photographs," in *Proceedings of the IEEE/CVF conference on computer vision and pattern recognition*, 2019, pp. 1712–1722.